Supplemental Information

Critical Influence of Cosolutes and Surfaces on the Assembly of Serpin-Derived Amyloid Fibrils

Michael W. Risør, Dennis W. Juhl, Morten Bjerring, Joachim Mathiesen, Jan J. Enghild, Niels C. Nielsen, and Daniel E. Otzen

SUPPORTING MATERIAL

Critical influence of co-solutes and surfaces on the assembly of serpin-derived amyloid fibrils

M.W. Risør, D.W. Juhl, M. Bjerring, J. Mathiesen, J.J. Enghild, N.C. Nielsen and D.E. Otzen

TABLE OF CONTENTS

SUPPORTING MATERIALS AND METHODS

THEORETICAL SECTION

Time-evolution of a fibrillating system

The time evolution of a fibrillating system can be described as a combination of the rate constants for the primary (k_n) and secondary (k_2) nucleation pathways, and fibril elongation (k_+). Primary nucleation pathways display strong monomer dependence and result in polynomial growth of aggregate mass, $M(t) \sim \lambda^2 t^2$ with $\lambda = \sqrt{2k_+ k_n m^{n_c}}$ where M is the aggregate mass, m is the monomer concentration, and n_c is the nucleus size. Secondary pathways represent processes that depend on the total aggregate mass such as nucleation sites on the fibrillar surface or fibril fragmentation, and result in exponential growth with a clear lag-phase owing to the autocatalytic term $M(t) \sim \exp(\kappa t)$ with $\kappa = \sqrt{2k_+ k_2 m^{n_2 + 1}}$ (1-3). The monomer dependence of the fibrillation reaction is reflected by a power-law relationship, $t_{1/2} = m_0^{\gamma}$, where $t_{1/2}$ represents the time to reach half-maximal aggregate mass (could also be lag-time, t_{lag}) and m_0 is the initial monomer concentration. The scaling exponent, γ, conveniently captures the effects of either λ or κ. As a result, the scaling exponent can take form of either $\frac{-n_c}{2}$ for primary nucleation (reflecting λ) or $\frac{-(n_c - 1)}{2}$ for secondary nucleation (reflecting κ). If monomer-independent processes such as fibril fragmentation dominate, the exponent can display weaker monomer dependence approximating $-\frac{1}{2}$ which represents the specialized case where $n_2 = 0$ (1-3). Importantly, primary nucleation can be catalyzed by surfaces (heterogeneous nucleation) which lower the energy barrier for the self-association process. Secondary pathways involve both monomer-dependent and -independent terms, in which secondary nucleation at the fibrillar surface represents the former, and filament fragmentation represents the latter. See Knowles and coworkers for additional details about the microscopic rate constants and the closed analytical solutions used to model amyloid growth phenomena (1, 2, 4, 5).

Heparin charge fraction calculation using counterion condensation theory

Heparin is a polyanion subject to counterion condensation in which a layer of condensed and mobile counterions results in a constant critical net charge density. The structural charge is reduced to a mean effective charge fraction, f_{av}, per polyion charge, which is the average of the charge fraction, $f(s)$, for each charge site, P, along the polymer of length L. For end segments,

where the charge's distance from the end is smaller than the Debye screening length, f(s) is expressed as (6): $f(s) = \frac{1}{2z\xi}\left(1 - \frac{\ln \kappa b}{\ln s/b}\right)$, where z is the charge per site, ξ is the charge density parameter, κ is the inverse of the Debye screening length, b is the axial spacing between neighboring charged groups, b = (P-1)/L, and s is the distance from the end. For the interior of the polymer, s > 1/κ , f(s) is a constant charge fraction expressed as (7): f(s)= 1/(zξ). A convenient formula for the Debye screening length as a function of ionic strength, I, is 1/κ = $0.305 I^{1/2}$, which is valid in water at room temperature with a Bjerrum length (l_b) of 0.71 (6). The charge density is expressed as $\xi = l_b/b$. We calculated f_{av} for native heparin assuming an average of 24 disaccharides per heparin chain (89 structural charges). With a disaccharide length of 1.02 nm (8), b = 0.28 nm, and ξ = 2.55. For an ionic strength of 10 mM, 1/κ = 3.05 nm, and f_{av} = 0.44 with the interior polymer f(s) defined > 12 charge sites from the end. For an ionic strength of 200 mM (PBS), 1/κ = 0.68 nm, and f_{av} = 0.42 with the interior polymer f(s) defined > 3 charge sites from the end. The resulting sodium counterion fractions (1-f_{av}) are θ_{Na} = 0.56 and 0.58 at I = 10 and 200 mM, respectively, which agree with experimentally determined values (9). With a sodium mass contribution of 48 Da per disaccharide (I = 10 mM) and a heparin disaccharide average unit mass of 591 Da (see main text), we get the average heparin$_{DS}$ with counterions = 605 Da. We used this mass for calculations of the heparin concentration. The molecular weight of 24 heparin$_{DS}$ units with counterions is 14.5 kDa which agrees with the M_n = 14.1 kDa found in the extensive MALS analysis of unfractionated heparin by Beirne et al. (10).

EXPERIMENTAL SECTION

pH-dependent fibrillation of C-36

Fibrillation reactions of 8 µM C-36 in PBS adjusted to pH 4.0, 5.0, 6.0, 7.0, 8.0, and 9.0 were carried out in half-area 96-well PS microplates with 40 µM ThT. The resulting ThT traces were normalized to the maximally obtained fluorescence value within the experimental window of 30h.

Quantification of residual C-36 monomer

Fibrillation reactions of 8 µM C-36 in PBS, pH 7.42, were prepared in half-area 96-well PS microplates with 40 µM ThT. The supernatant was pooled from three reactions for eight different time points during fibrillation. Gel filtration analysis was performed on 200 µL of the supernatant using a Superdex Peptide column equilibrated in PBS. The residual monomer amount was quantified by the integrals of the eluted monomeric C-36 peak.

Preparation of ThT traces for global fitting

The global fitting to models of primary and secondary nucleation was carried out using averaged ThT curves. These curves were generated by shifting each experimental ThT trace to the average $t_{1/2}$ of the triplicate, followed by averaging of each shifted triplicate. This ensured a correct representation of the curve profile which otherwise would have been skewed for some concentration points due to the lag-time variations within the triplicates.

Seeded C-36 fibrillation

C-36 (16 µM) was fibrillated in PS and NBS plates under quiescent conditions for two days to generate PS and NBS fibrils for seeds. ThT levels were monitored to validate the fibrillation reaction was complete. The seed material was prepared by extracting fibrils from the plates by thorough pipetting, followed by bath sonication for 10 min. Before sonication, a small fraction of the NBS and PS fibrillar seed material was analyzed by transmission electron microscopy (TEM) to validate the fibrillar seed morphology. Seeded reactions were prepared with 8 µM C-36 using seed concentrations ranging from 0-16%. Each condition was conducted in triplicate and the assay was repeated twice to verify consistent results. Fibril elongation rates for both seed types were extracted during the initial phase of the reactions (< 25 min).

Heparin addition to C-36 during fibrillation

Multiple C-36 fibrillation reactions (10 µM, 150 µL) were conducted in PS plates in PBS and the

ThT signals were monitored. Heparin was added (50 µg/mL, 8:1 heparin$_{DS}$:peptide) to reactions at seven different time points when ThT levels had reached ~ 0, 10, 25, 50, 75, 82, 93, and 96% of the final endpoint value. The reactions were allowed to proceed for 24h. Heparin additions were done in triplicate at every time point and the endpoint fibrils were harvested, redissolved in H$_2$O, and analyzed by TEM. Because ribbon twist fibrils dominated the PS surface and heparin induced curvilinear fibrils, we could visualize the contribution from each fibrillation pathway by TEM.

Heparin effect on ThT fluorescence from pre-formed C-36 fibrils

C-36 was fibrillated in NBS plates (8 µM reactions) in the presence of ThT (40 µM) for 48h. The effect of heparin on the endpoint ThT fluorescence was assessed by adding heparin (10 µg/mL to 200 µg/mL) to the C-36 reactions. The endpoint ThT fluorescence reduction was assessed after 50 min of equilibration and plotted as a function of heparin concentration.

FITC-heparin association with C-36 fibrils

We mixed 35 µM or 5 µM fluorescein isothiocyanate (FITC)-labeled heparin with pre-formed C-36 fibrils. Different FITC-heparin solutions were used to sample both high and low heparin$_{DS}$:peptide ratios using the same fibril stock. C-36 fibrils were formed by three days incubation in PBS at 50 µM peptide concentration. We confirmed that the FITC-heparin signal in the supernatant with C-36 fibrils was reduced compared to the supernatant without C-36 fibrils. The ratio of bound heparin (in units of disaccharide, heparin$_{DS}$) per C-36 monomer was calculated based on a FITC-heparin standard curve. The FITC-heparin disaccharide concentrations were calculated by using the heparin$_{DS}$ MW of 605 Da and did not account for the FITC-moiety's mass contribution. Reactions were mixed in a total volume of 50 µL, incubated for 2h at 37 °C, and then spun down at 15,000 g. The supernatant was transferred to a 96-well half-area plate and diluted twice. The fluorescence signal from the residual FITC-heparin in solution was monitored on an Omega Fluostar plate reader with 485 nm excitation and 520 nm emission filters.

Fourier Transform Infrared Spectroscopy (FT-IR)

FT-IR spectra were measured on monomer and fibrillar C-36 material using a Tensor27 FTIR spectrometer (Bruker) equipped with attenuated total reflection accessory with a continuous flow of N$_2$ gas. The material was spotted into the target plate and dried under nitrogen flow before recording the spectra, and 128 scans were averaged for each spectrum. After compensation for

atmospheric contributions, the absorbance was depicted relative to the largest peak intensity and peak positions were identified from second derivative analysis.

Liquid-state NMR experimental details

Samples for liquid-state NMR were prepared at 200 μM C-36 with 20 mM Na_2HPO_4, pH 7.0 (PB buffer), and 20 mM HEPES, pH 7.0 (HEPES buffer). We added 8% D_2O (v/v) for the lock and 50 μM DSS for referencing. The inert paramagnetic agent, FeDO3A, was added to both samples to reach a final concentration of 10 mM for rapid acquisition through paramagnetic relaxation enhancement, as previously reported (11). The samples were mixed at 4 °C to prevent premature aggregation. All experiments were carried out at 5 °C using a Bruker 500 MHz spectrometer. We conducted ^1H-^{15}N-HSQC experiments with a recycle delay of 100 ms, 2048 (^1H) x 256 (^{15}N) complex points, 32 ppm spectral width (^{15}N), and a carrier at 117 ppm. Experiment time was less than 5 min for each individual spectrum, excluding the effect of aggregate formation on the spectral quality and dispersion.

Solid-state NMR experimental details

Uniformly (^{15}N-^{13}C)-labeled non-heparin fibrils (N-fibrils) and heparin-fibrils (H-fibrils) were formed in standard polypropylene tubes (15 mL and 50 mL) and resulted in complete monomer depletion and morphological appearances comparable to recombinant C-36 fibrils formed in PS plates with and without heparin. The fibrils were spun down at 50.000 g and resuspended in 10 mM PB buffer (N-fibrils) or 10 mM PB buffer with 100 μg/mL heparin (H-fibrils). We recorded ssNMR spectra at 1 °C at 12 kHz magic angle spinning on a 700 MHz Bruker spectrometer. To probe potential mobile regions of N-fibrils, we acquired 1D CP and refocused INEPT with ^1H decoupling with 4096 direct points, 512 scans, and equal receiver gains for comparison. This strategy has successfully revealed mobile regions of other fibril systems (12, 13). The ^{13}C-^{13}C correlation DARR experiments for N- and H-fibrils were each carried out with 4K x 256 complex points, 80 scans per increment, 200 ppm indirect spectral width, a carrier frequency at 100 ppm, and 80 kHz Spinal-64 ^1H decoupling (14). Processing was done with 4K x 256 points, an EM window function with LB set to 50 Hz (direct) and 30 Hz (indirect), the GB set to 0 (direct) and 0.1 (indirect), and SSB set to 2 for both dimensions. We referenced the spectra to TMS using an external sample of adamantane with the CH_2 signal at 38.48 ppm.

Proteolytic susceptibility of fibrils

C-36 fibril and monomer samples (~2 µg) were incubated for 2h with thermolysin or trypsin at the indicated stoichiometry to address the degree of resistance towards proteolysis in the amyloid fibrils. We evaluated the products were using tricine gels for optimal separation of low molecular weight products.

SUPPORTING FIGURES S1-S14
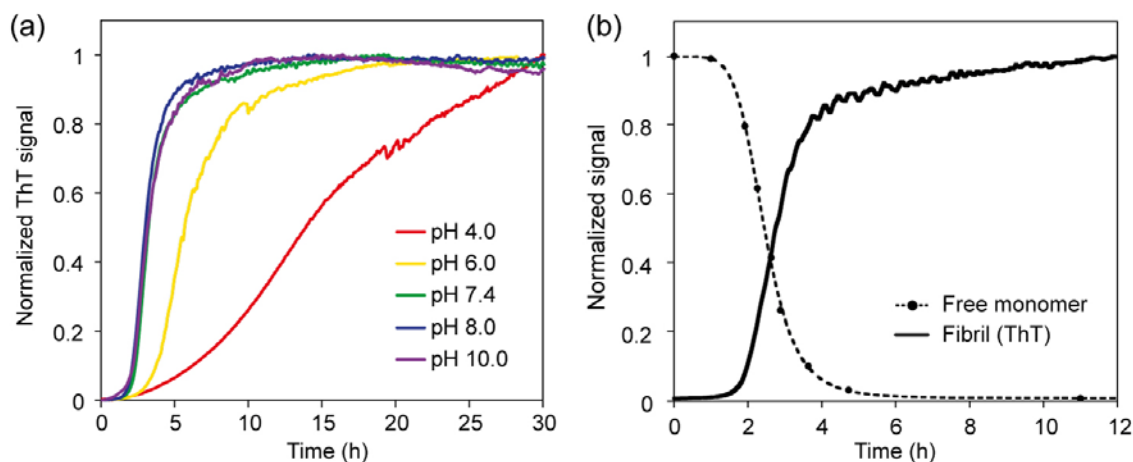
FIGURE S1 C-36 fibrillates at physiological pH and leads to monomer depletion
(a) Normalized traces of C-36 fibril formation (8 µM) by ThT fluorescence at the indicated pH values in PBS using PS plates. (b) Fibrillation by ThT fluorescence (8 µM C-36 in PBS, pH 7.42) leads to monomer depletion. The free monomer concentration was measured by gel filtration.
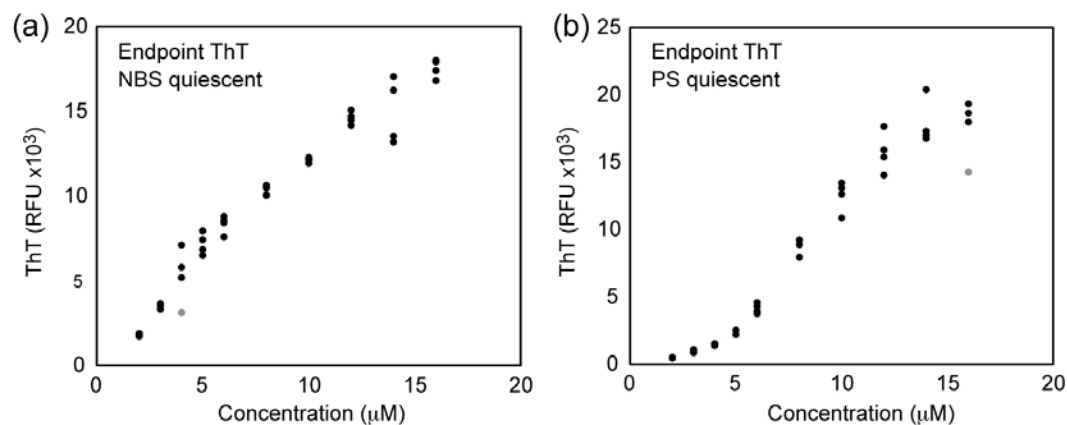
FIGURE S2 Correlation of the endpoint ThT with the C-36 concentration
Fibrillation was conducted on NBS and PS plates for various C-36 concentrations as shown in Fig. 1 (main text). (a) For NBS plates, the endpoint ThT level (after 92 h) correlated relatively well with the C-36 concentration. (b) For PS plates, lower peptide concentrations had a slightly smaller relative fluorescence compared to higher concentrations. This could be caused by a critical C-36 concentration below which monomers did not continue to associate with the fibril mass. For the kinetic treatments, we assumed that all peptide was full converted to aggregate mass at the ThT plateau level.
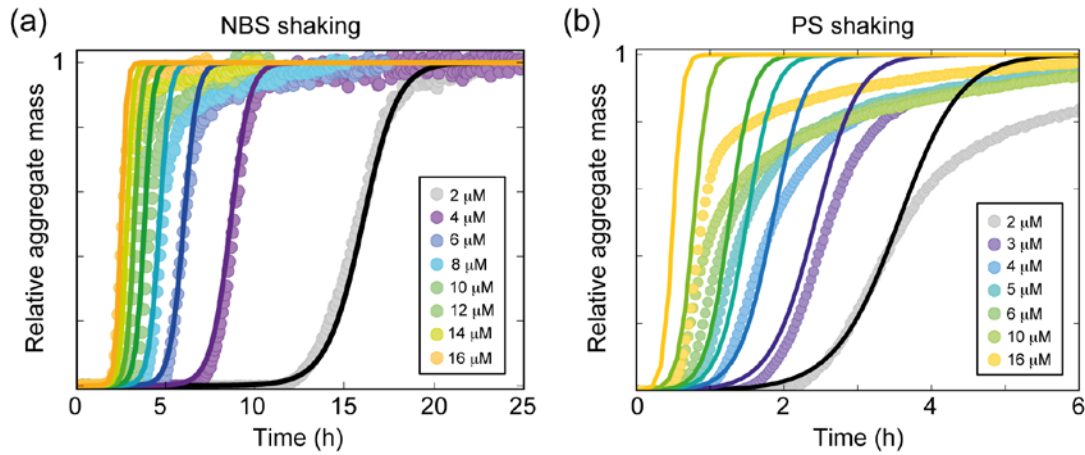
FIGURE S3 Global SP model fits to aggregate mass under shaking conditions
(a) Global fit to NBS shaking ThT traces using the SP-model with both primary and secondary nucleation. The nucleus size for secondary nucleation (n_2) was set to 0.78, derived from the γ_{NBS-S} scaling exponent of -0.88 that was valid for the entire concentration range. The nucleus size for primary nucleation (n_c) was set to 1.85, similar to the SP model for the NBS quiescent data. The extracted values for the secondary and primary nucleation contribution were $k_+k_2 = 6.5\cdot10^9$ and $k_+k_n = 7\cdot10^3$. The NBS shaking ThT traces displayed a steep ThT signal increase after the initial lag phase and rapidly reached plateau values compared to fibrillation under quiescent conditions. This "sawtooth" time profile can arise from a multi-exponential monomer-independent process such as filament breakage (1, 3). (b) Global fit to PS shaking ThT traces using the SP model with n_2 set to 0.82 (from a γ_{PS-S} scaling exponent of -0.91) and n_c fitted to 2.1. The extracted values for the secondary and primary nucleation contribution were $k_+k_2 = 6\cdot10^{10}$ and $k_+k_n = 1.5\cdot10^9$. The model only partially represented the data at low concentrations (2-6 µM) and could not explain the slower growth of aggregate mass after $t_{1/2}$. Introduction of shaking clearly accelerated the ordered amyloid conversion but because the nature of the dominating nucleation term was unaltered ($\gamma_{PS-Q} \sim \gamma_{PS-}$), the PS surface may prevent fragmentation from becoming a strong secondary pathway.
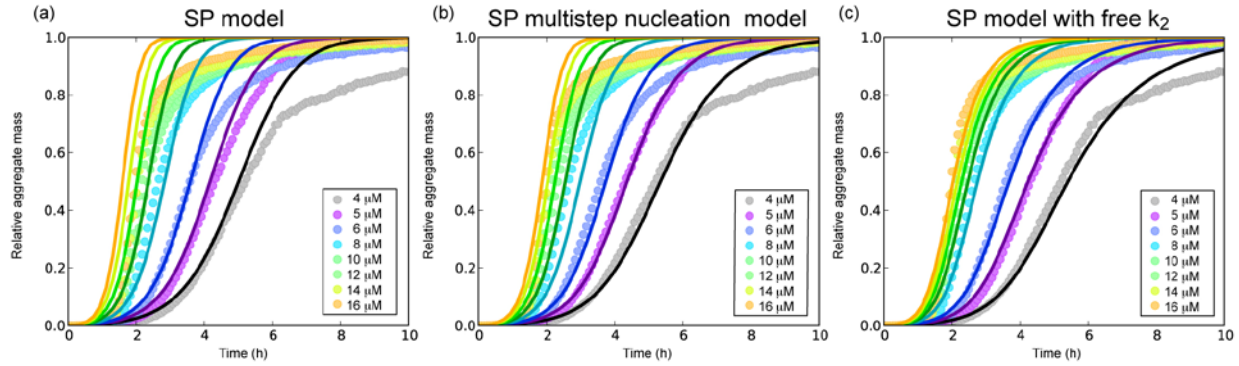
FIGURE S4 Alternative SP model fits to C-36 PS quiescent data

(a) The simple SP model fit. New aggregates (P) are generated according to (5): $\frac{dP}{dt} = k_n[m]^{n_c} + k_2[m]^{n_c}[M]$ with n_c = 1.43, n_c = 0.76, k_+k_n= 2.0·10^9, and k_+k_n = 2.1·10^5. (b) The secondary pathway model with multistep nucleation model fit. In brief, this model incorporates a saturation term, K_m, which scales the new aggregate formation from secondary nucleation with the monomer concentration in a Michaelis-Menten-like fashion (15): $\frac{dP}{dt} = k_n[m]^{n_c} + k_2 \frac{[m]^{n_c}}{1+[m]^{n_c}/K_m}[M]$. The model was globally fitted to the experimental traces with n_c=1.44, n_2=2, k_+k_n,= 2.0·10^5, k_+k_2 = 2.0·10^{16}, and K_m = 1.7·10^{-11}. K_m is given in units of $conc^{n_2}$ and by using the value of n_2, we get a meaningful midpoint for the saturation (K_m in conc) at 4 µM. (c) The SP model with individual fits of the secondary rate constant, k_2k_+. The free parameter allows for much better agreement with the experimental curves but with a resulting loss of global information. The global parameters were n_c = 1.45, n_2 = 2.8, k_+k_n = 10^5 and the individual k_+k_2 parameters for 4, 8, 16 µM were 2.6·10^{20}, 8.2·10^{19}, and 9.2·10^{18}, respectively, which suggests a decrease of the secondary pathway contribution at higher C-36 concentrations. All fits were carried out with the Amylofit online tool (16).
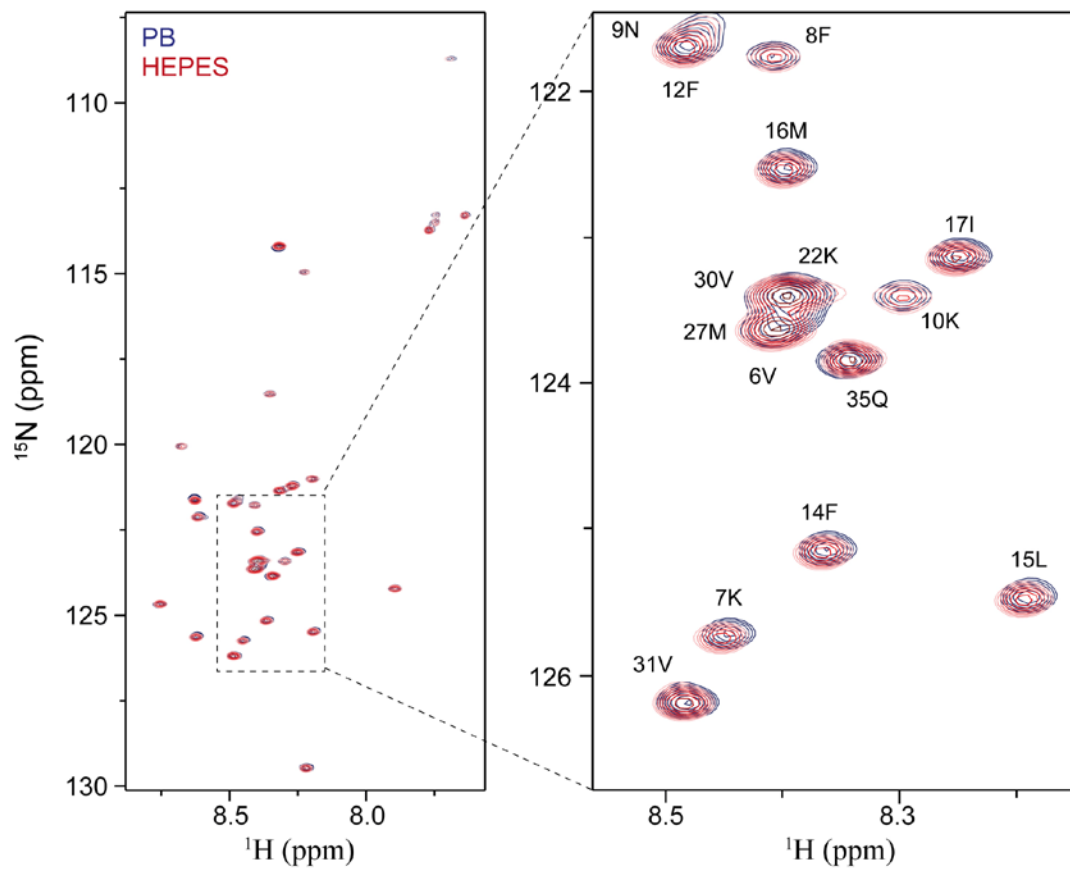
10

FIGURE S5 C-36 shows similar chemical shift correlations in PB and HEPES buffer
Liquid-state NMR ¹H-¹⁵N-HSQC for C-36 in PB (blue) and HEPES (red) buffer recorded at 5 °C
with a peptide concentration of 200 µM. Resonances corresponding to various backbone amides
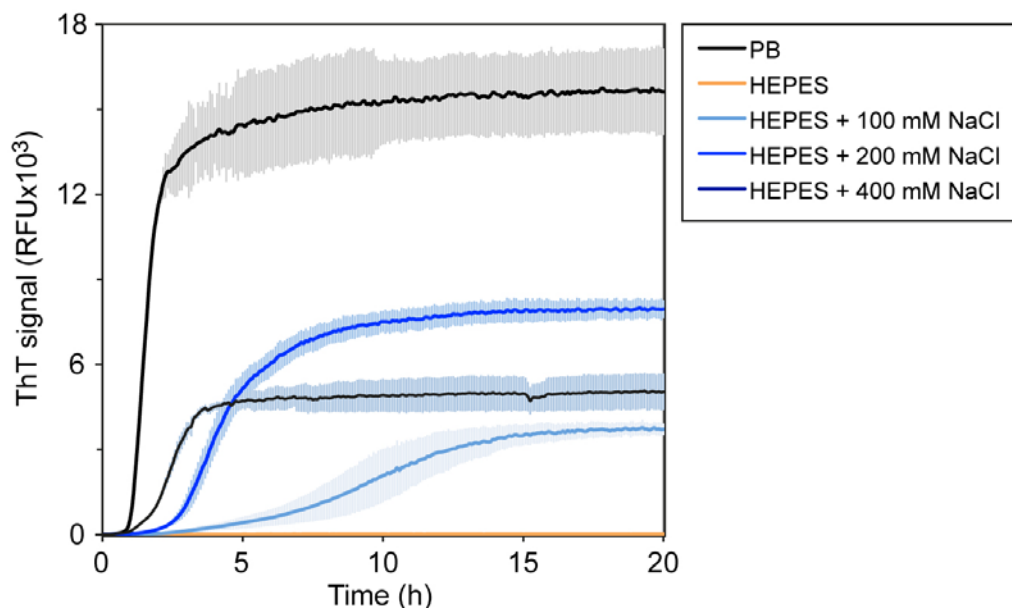across the C-36 sequence are indicated for the zoomed region.

FIGURE S6 Sodium Chloride potentiates C-36 fibrillation in HEPES buffer
C-36 reactions (8 µM) were set up in HEPES buffer in PS plates with the indicated amount of NaCl. A set of reactions were set up in PB buffer for comparison. Error bars represent the triplicate point standard deviation.

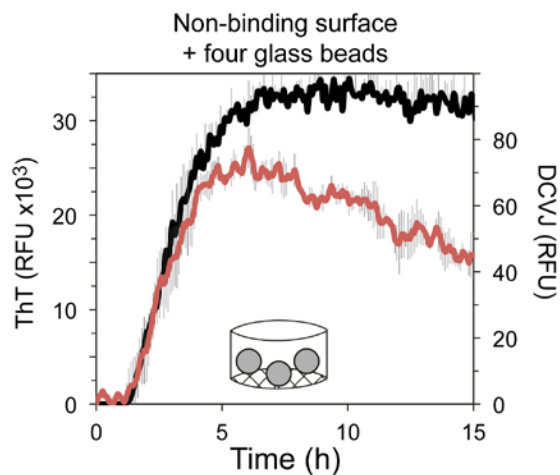***FIGURE S7 DCVJ signal follows the ThT trace in the presence of glass beads***
ThT and DCVJ fluorescence was measured for 16 µM C-36 fibrillation reactions in NBS plates in the presence or absence of four silica glass beads (ø = 1 mm). The DCVJ signal (red) was similar to the ThT signal (black), ruling out pre-ThT hydrophobic species. Grey error bars indicate the triplicate standard deviation for each point.
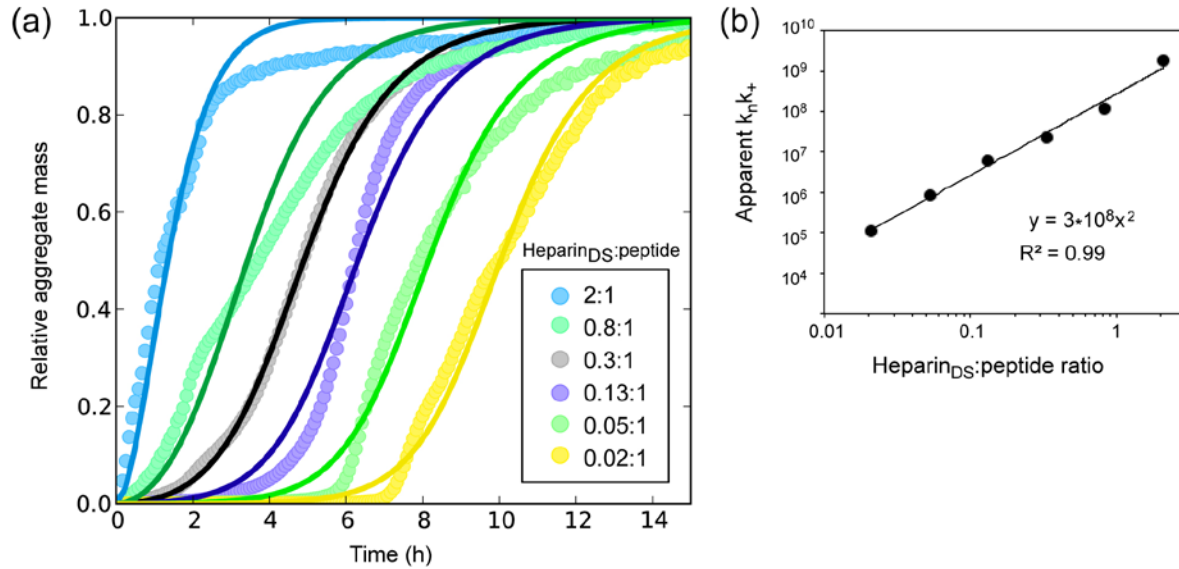
FIGURE S8 Heparin stimulates C-36 fibrillation by enhancing primary nucleation.

(a) The major features of the heparin-stimulated C-36 fibrillation in NBS for heparin$_{DS}$:peptide ratios from 0.02 to 0.20 could be captured by the SP model. Nucleus sizes were set to the values found for the global SP fit to C-36 in NBS, which were $n_c = 1.85$ and $n_2 = 1.9$. The secondary nucleation rate constant was globally fitted to 3.8E-8 and the apparent primary nucleation rate was fitted to each curve individually. (b) The primary nucleation rate constant appeared as a function of the heparin$_{DS}$:peptide ratio squared, illustrating a clear stimulation of this nucleation constant by heparin. If we consider the generation of new aggregates by both homogenous and heparin-accelerated heterogeneous primary nucleation, we get an expression as follows: $\frac{dP}{dt} = k_n m_0^{n_c} + k_H m_0^{n_c} H^{n_H} = k_n(k_H + H^{n_H}) \cdot m_0^{n_c}$, where H denotes heparin. Under the assumption that heparin contributes with this type concentration-dependent rate enhancement, we can consider the individual fit values of the primary nucleation rate constant in the SP model as apparent rate constants, $k_{app} = k_n(k_H + H^{n_H})$. From this expression, we find the expected power-law scaling behavior of k_{app} as a function of H with a reaction coefficient of n_H, which was determined to be 2.0 for heparin's stimulation of C-36 fibrillation.
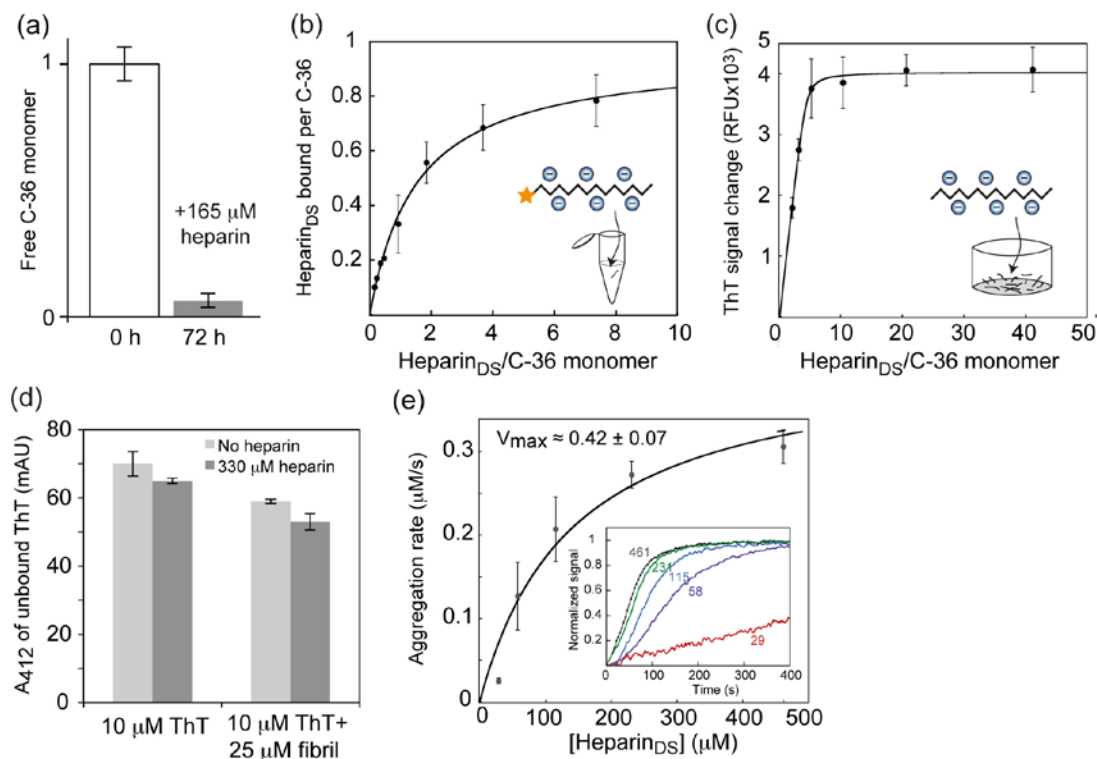
13

FIGURE S9 Heparin associates with C-36 aggregates and alters ThT fluorescence
(a) Residual monomer was quantified by gel filtration before and after incubation with heparin for 72 h. (b) FITC-heparin binding per C-36 monomer (R_H), as a function of the heparin$_{DS}$:peptide ratio (R_{H0}). The binding was quantified by the residual FITC-heparin amount left in the supernatant after co-incubation with fibrils for 1 h. Fitting was done with the equation $R_H = R_{H0}*R_{max}/(K_d+R_{H0})$, resulting in an R_{max} of 0.96 ± 0.03 (c) ThT fluorescence change of pre-formed C-36 fibrils as a function of the added heparin amount, expressed as the heparin$_{DS}$_peptide ratio. Larger variations are seen due to variations in the actual endpoint ThT level of the in-plate pre-formed C-36 fibrils. (d) Quantification of the unbound ThT by absorbance at 405 nm in the presence of heparin and C-36 fibrils. Heparin does not diminish the ThT binding to fibrils. (e) Time-course profiles for the change in β-sheet content at 222 nm were recorded for heparin$_{DS}$:peptide ratios ranging from 1.2:1 to 18.5:1 (29-461 μM of heparin$_{DS}$). Extracted C-36 aggregation rates were plotted as a function of heparin concentration. Insert shows normalized CD signal change for indicated heparin$_{DS}$ concentrations.
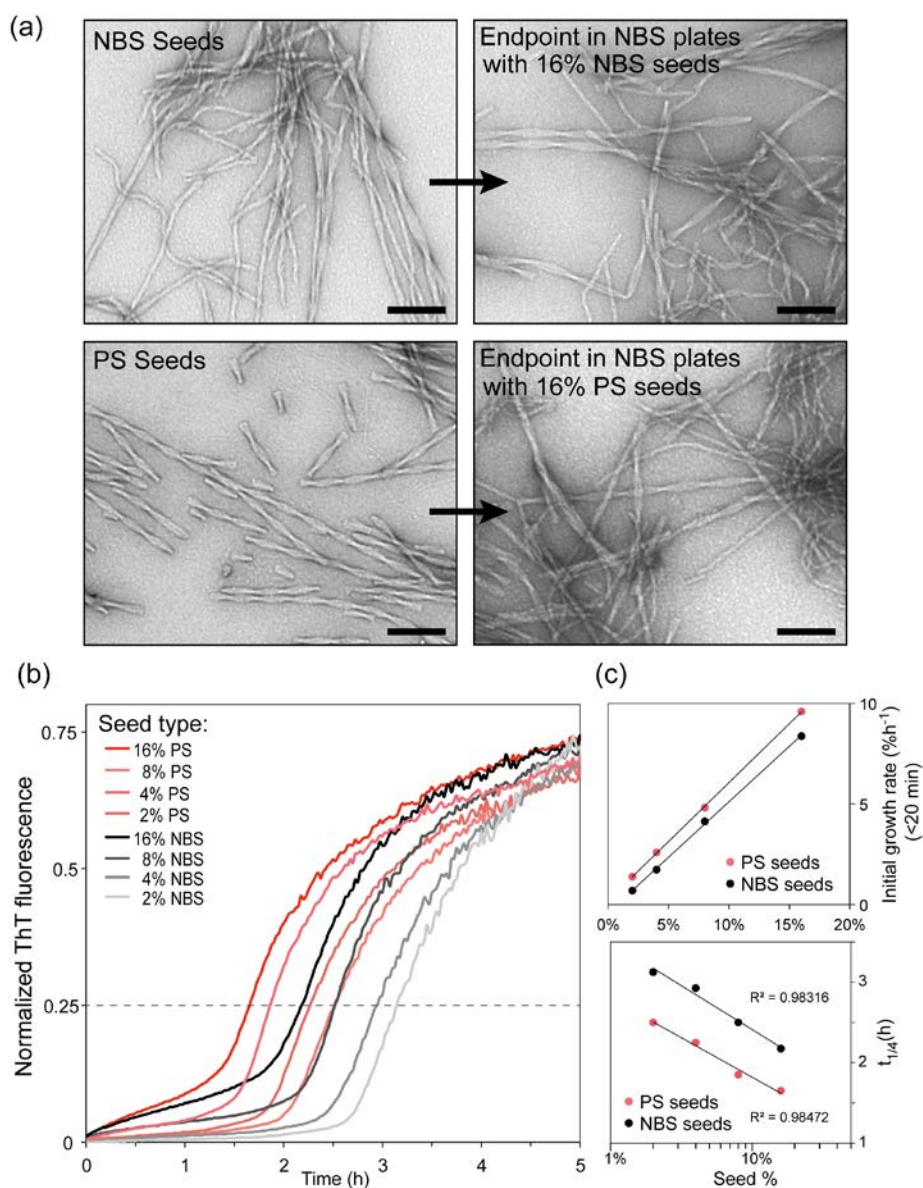
FIGURE S10 Surface-generated twisted ribbon seeds accelerate bulk nucleation

(a) TEM images of the NBS and PS fibril populations used for seeds (left) and the endpoint species observed after fibrillation in NBS plates in the presence of 16% of either seed type (right). (b) Triplicate average ThT traces after the addition of the indicated seed amount to 8 µM C-36 and subtraction of the initial ThT value. (c) For both NBS and PS seeds, the initial fibril growth rates (<25 min) correlated linearly with the seed amount (top) and the addition of seeds caused a semi-log scaling behavior of $t_{1/4}$ as a function of seed concentration (bottom) (2, 17). The dashed line in (b) represents the 25% value of the normalized ThT traces from which $t_{1/4}$ is derived. We used $t_{1/4}$ in place of $t_{1/2}$ that did not accurately reflect the fibrillation growth phase in this case. PS seeds stimulated secondary pathways (smaller $t_{1/4}$ values) slightly better than NBS seeds. This may indicate that the ribbon-twist morphology had a higher secondary nucleation potential than alternate NBS morphologies, in line with observed differences in co-existing polymorphs' seeding ability for other amyloid systems such as Aβ (18, 19).
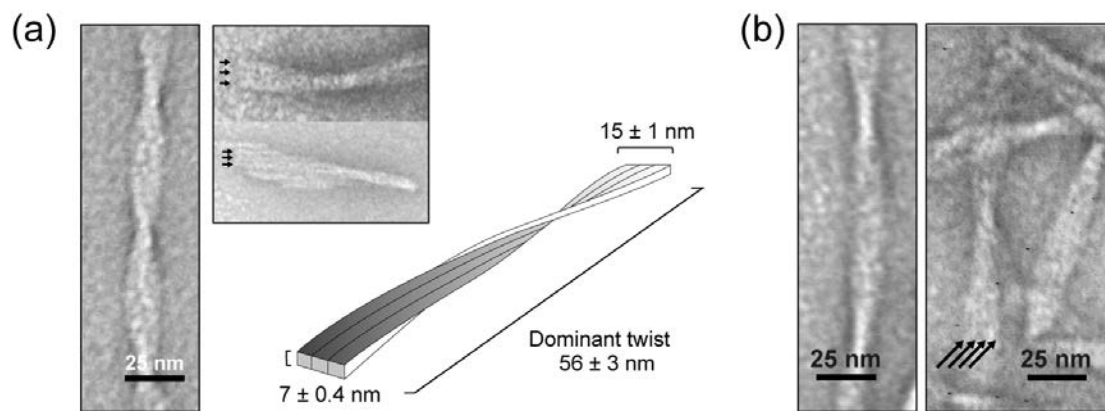
FIGURE S11 Ribbon morphology details for PS and glass-induced C-36 fibrils

(a) The ribbon twist morphology of PS fibrils consisted of three twisting laterally associated protofibrils (indicated by arrows) with a ribbon width of 15 nm. The lateral association is also illustrated by a sheet of fibrils occurring under high agitation. Graphic shows a model fibril with measured fibril dimensions (n = 50) (b) Glass-induced fibrils had a larger width of 16 nm, a twist periodicity of 89 nm, and consisted of four laterally associated protofibrils (indicated by arrows).
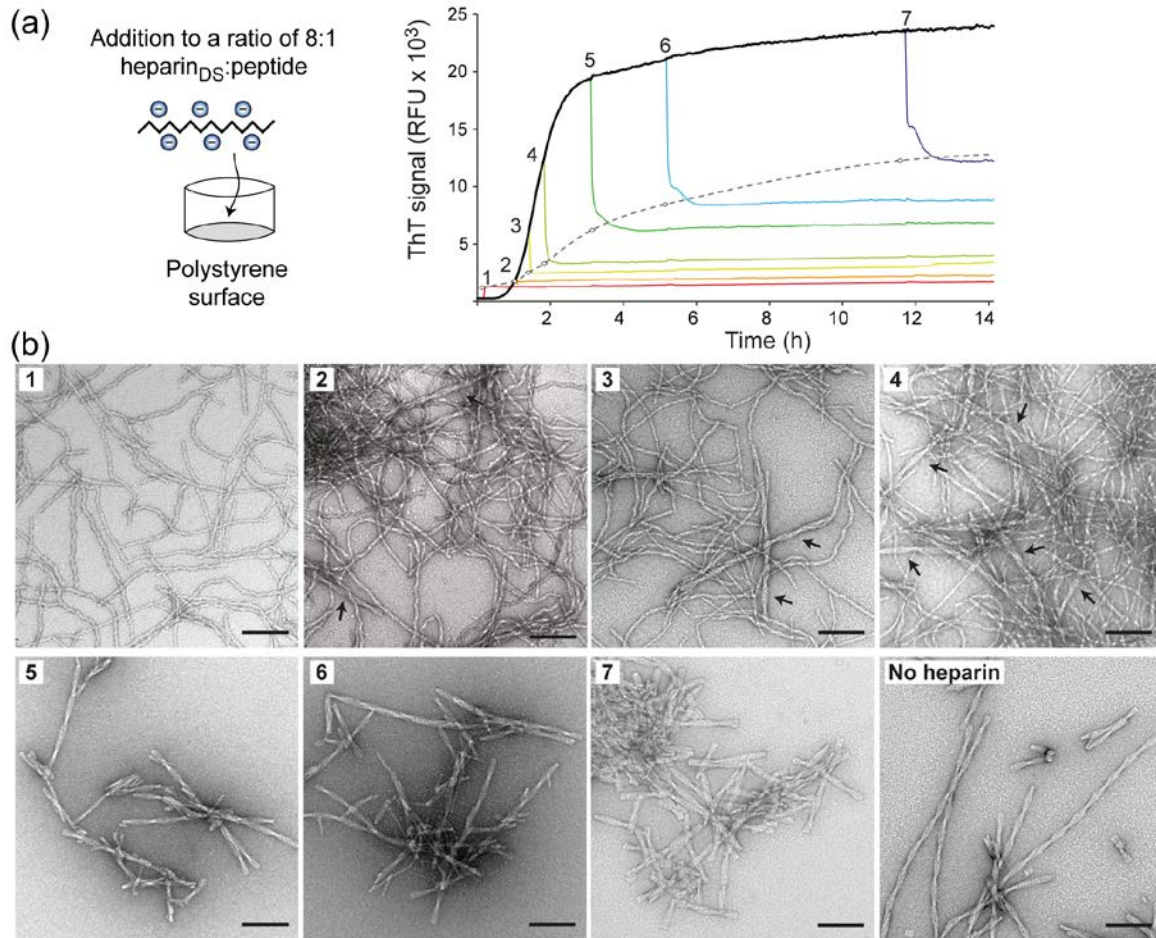
(a) Addition to a ratio of 8:1 heparin$_{DS}$:peptide

Polystyrene surface

(b)

1 | 2 | 3 | 4
5 | 6 | 7 | No heparin

FIGURE S12 Heparin remodels monomeric C-36 and binds existing fibrils

(a) ThT traces after indicated additions of heparin to the ongoing fibrillation reactions of 10 µM C-36 in PS plates. Heparin modulates the ThT fluorescence level for all additions but the effect was diminished at later time points with higher ThT levels. The plateau ThT level reached for each heparin addition is indicated by circles which are connected by a stapled line to illustrate the saturation behavior (b) Morphology of the amyloid fibrils at the end of the fibrillation reaction (20 h). Arrows indicate the presence of ribbon twist fibrils for images 2-4. The amount of ribbon twist fibrils correlated with the ThT level increase before heparin addition. No effect of heparin on fibril morphology is seen when heparin is added to C-36 reactions that approached the ThT plateau (images 5-7).
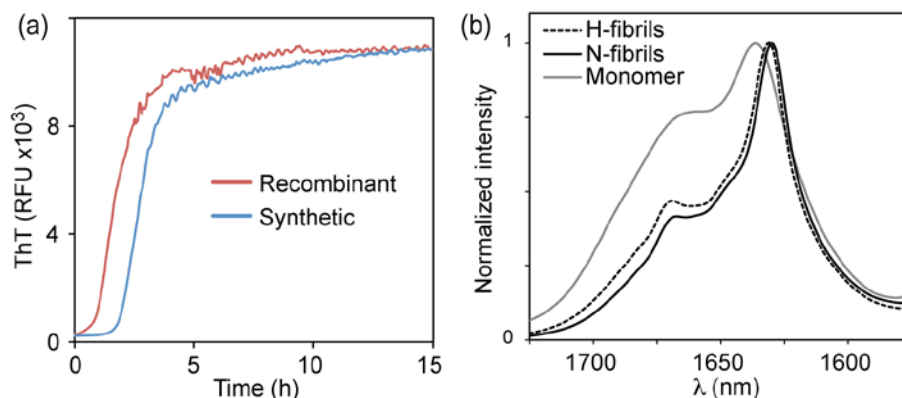
FIGURE S13 Fibrillation of recombinant and synthetic C-36 and comparison of heparin- and non-heparin fibrils by FTIR

(a) ThT traces of 8 µM recombinant and synthetic C-36 suggest similar fibrillation behavior. (b) FT-IR spectra in the amide I region from 1600-1700 nm of heparin-induced and non-heparin amyloid fibrils (H- and N-fibrils) was similar with a peak centered at 1630 nm, which is in the classic amyloid β-sheet H-bonded carbonyl stretching frequency range (20). The monomeric C-36 had a different spectral profile and displayed partial β-sheet characteristics in this water-removed dry state.
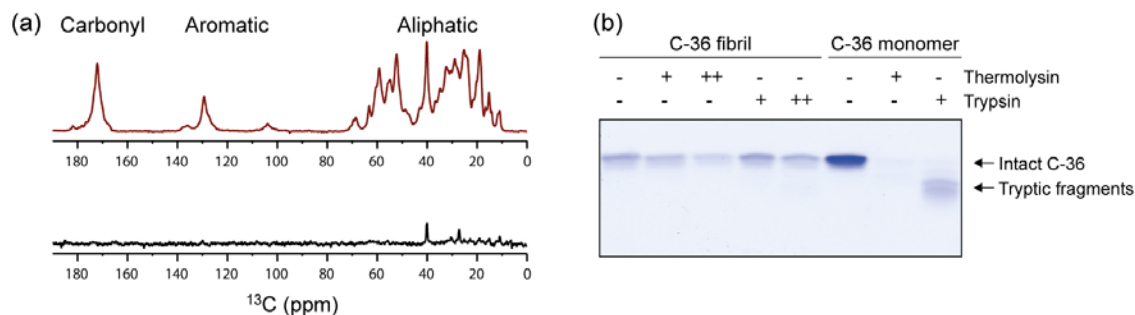

FIGURE S14 ssNMR 13C-signals and proteolytic protection support full fibril incorporation of the C-36 sequence

(a) ^{13}C-signals from the solid region of C-36 fibrils measured by a dipolar-based cross-polarization ssNMR experiment (top) and ^{13}C-signals from the mobile region of C-36 fibrils measured by a J-coupling-based INEPT-like ssNMR experiment (bottom). The lack of any significant signals above noise in the J-coupling-based experiment suggested incorporation of all the C-36 residues into the solid-phase fibril arrangement. (b) 3 µg of monomeric and fully fibrillated C-36 were subjected to proteolysis by thermolysin or trypsin for 2 h. C-36 contains three internal tryptic sites, K7, K22, and K29. While the monomer was completely digested within this time frame, the fibrillar form largely resisted proteolysis, suggesting a lack of proteolytically accessible flexible loops and full incorporation of the entire peptide sequence into an amyloid structure.

SUPPORTING REFERENCES

1.   Cohen, S. I., M. Vendruscolo, C. M. Dobson, and T. J. Knowles. 2013. The Kinetics and Mechanisms of Amyloid Formation. In Amyloid Fibrils and Prefibrillar Aggregates: Molecular and Biological Properties. D. E. Otzen, editor. Wiley-VCH Verlag GmbH & Co. KGaA.

2.   Knowles, T. P. J., C. A. Waudby, G. L. Devlin, S. I. Cohen, A. Aguzzi, M. Vendruscolo, E. M. Terentjev, M. E. Welland, and C. M. Dobson. 2009. An analytical solution to the kinetics of breakable filament assembly. Science 326:1533-1537.

3.   Cohen, S. I., S. Linse, L. M. Luheshi, E. Hellstrand, D. A. White, L. Rajah, D. E. Otzen, M. Vendruscolo, C. M. Dobson, and T. P. Knowles. 2013. Proliferation of amyloid-beta42 aggregates occurs through a secondary nucleation mechanism. Proc Natl Acad Sci U S A 110:9758-9763.

4.   Cohen, S. I. A., M. Vendruscolo, C. M. Dobson, and T. P. J. Knowles. 2012. From macroscopic measurements to microscopic mechanisms of protein aggregation. J Mol Biol 421:160-171.

5.   Cohen, S. I. A., M. Vendruscolo, M. E. Welland, C. M. Dobson, E. M. Terentjev, and T. P. J. Knowles. 2011. Nucleated polymerization with secondary pathways. I. Time evolution of the principal moments. J Chem Phys 135:065105.

6.   Manning, G. S. 2008. Approximate Solutions to Some Problems in Polyelectrolyte Theory Involving Nonuniform Charge Distributions. Macromolecules 41:6217-6227.

7.   Manning, G. S. 1969. Limiting Laws and Counterion Condensation in Polyelectrolyte Solutions I. Colligative Properties. The Journal of Chemical Physics 51:924-933.

8.   Diakun, G. P., H. E. Edwards, D. J. Wedlock, J. C. Allen, and G. O. Phillips. 1978. The Relationship between Counterion Activity Coefficients and the Anticoagulant Activity of Heparin. Macromolecules 11:1110-1114.

9.   Rabenstein, D. L., J. M. Robert, and J. Peng. 1995. Multinuclear magnetic resonance studies of the interaction of inorganic cations with heparin. Carbohydrate research 278:239-256.

10.   Beirne, J., H. Truchan, and L. Rao. 2011. Development and qualification of a size exclusion chromatography coupled with multiangle light scattering method for molecular weight determination of unfractionated heparin. Anal Bioanal Chem 399:717-725.

11.   Oktaviani, N. A., M. W. Risor, Y. H. Lee, R. P. Megens, D. H. de Jong, R. Otten, R. M. Scheek, J. J. Enghild, N. C. Nielsen, T. Ikegami, and F. A. Mulder. 2015. Optimized co-solute paramagnetic relaxation enhancement for the rapid NMR analysis of a highly fibrillogenic peptide. J Biomol NMR 62:129-142.

12.   Hu, K.-N., R. P. McGlinchey, R. B. Wickner, and R. Tycko. 2011. Segmental polymorphism in a functional amyloid. Biophys J 101:2242-2250.

13.   Kryndushkin, D. S., R. B. Wickner, and R. Tycko. 2011. The core of Ure2p prion fibrils is formed by the N-terminal segment in a parallel cross-β structure: evidence from solid-state NMR. J Mol Biol 409:263-277.

14.   Fung, B. M., A. K. Khitrin, and K. Ermolaev. 2000. An improved broadband decoupling sequence for liquid crystals and solids. J Magn Reson 142:97-101.

15.   Meisl, G., X. Yang, E. Hellstrand, B. Frohm, J. B. Kirkegaard, S. I. A. Cohen, C. M. Dobson, S. Linse, and T. P. J. Knowles. 2014. Differences in nucleation behavior underlie the contrasting aggregation kinetics of the Aβ40 and Aβ42 peptides. Proc Natl Acad Sci USA 111:9384-9389.

16.   Meisl, G., J. B. Kirkegaard, P. Arosio, T. C. Michaels, M. Vendruscolo, C. M. Dobson, S. Linse, and T. P. Knowles. 2016. Molecular mechanisms of protein aggregation from global fitting of kinetic models. Nature protocols 11:252-272.

17.   Lorenzen, N., S. I. Cohen, S. B. Nielsen, T. W. Herling, G. Christiansen, C. M. Dobson, T. P. Knowles, and D. Otzen. 2012. Role of elongation and secondary pathways in S6 amyloid fibril growth. Biophysical journal 102:2167-2175.

18.   Paravastu, A. K., A. T. Petkova, and R. Tycko. 2006. Polymorphic fibril formation by residues 10-40 of the Alzheimer's beta-amyloid peptide. Biophys J 90:4618-4629.

19.   Petkova, A. T., R. D. Leapman, Z. Guo, W.-M. Yau, M. P. Mattson, and R. Tycko. 2005. Self-propagating, molecular-level polymorphism in Alzheimer's beta-amyloid fibrils. Science 307:262-265.

20.   Zandomeneghi, G., M. R. Krebs, M. G. McCammon, and M. Fandrich. 2004. FTIR reveals structural differences between native beta-sheet proteins and amyloid fibrils. Protein Sci 13:3314-3321.